PHYSICAL HYSTERESIS OF THE PIEZOELECTRIC DRIVE IN PRECISE IMAGE VELOCITY STABILIZATION SYSTEM BUILT INTO THE EARTH OBSERVING ORBIT TELESCOPE

Yevgeny Somov
Navigation, Guidance and Control
Samara State Technical University
Russia
e_somov@mail.ru

Sergey Butyrin
Navigation, Guidance and Control
Samara State Technical University
Russia
butyrinsa@mail.ru

Tatyana Somova
Navigation, Guidance and Control
Samara State Technical University
Russia
te_somova@mail.ru

Abstract

An image velocity stabilization system built into a space telescope for scanning optoelectronic observation of terrestrial targets with a physical hysteresis of a piezo-ceramic drive is considered. Elaborated algorithms for discrete filtering, results on analysis of the image motion velocity stabilization as well as technologies for terrestrial and in-flight verification are briefly presented.

Key words

Space telescope, Earth observation, an image velocity stabilization, piezoceramic drive, physical hysteresis.

Abbreviations

    ACS = Attitude Control System
    BRF = Body Reference Frame
    ICV = Image Cross Velocity
    ILV = Image Longitudinal Velocity
    IMC = Image Motion Compensator
    IMV = Image Motion Velocity
    IRF = Inertial Reference Frame
    OEC = Optoelectronic Converter
    OGS = Offset Guiding Sensor
    ORF = Orbital Reference Frame
    PCE = Piezoceramic Element
    TDI = Time Delay and Integration

1 Introduction

A correct mathematical description of physical hysteresis is a basic problem for an *internal friction theory* [Sorokin, 1960; Panovko, 1960; Palmov, 1976; Kochneva, 1979; Visintin, 2006; Dragan, 2006] et al. with regard to the well-known *flexible-plastic micro-deformations* of materials. The mathematical foundations for analysis of hysteresis models are presented in a number of special publications [Krasnosel'skii and Pokrovskii, 1989; Visintin, 2014], and their application to piezo drives – in articles [Zhang et al., 2012; Yu et al., 2020] et al. In the late 1990s, it was developed a universal approach to describing physical hysteresis [Somov, 2000; Somov, 2004] based on *set-valued* differential equations with discontinuous right-side. This article deals a precision image velocity stabilization system with a piezoelectric drive, built into the Earth observing orbit telescope [Somov et al., 2022]. Here, we briefly present new results on modeling the physical hysteresis of a piezo drive, original algorithms for digital processing measurements as well as the results of studying the considered cyber-physical system [Derler et al., 2012].

2 The Image Stabilization in a Space Telescope

Over the past three decades, a number of large space astronomical observatories have been created by NASA and ESA. The *Hubble Space Telescope* (*HST*) was carried into the near-circular orbit with altitude 559 km in 1990 and today remains in operation. The 2.4-meter aperture optical telescope has instruments for observing in the near ultraviolet, visible, and near infrared bounds. Here, the offset guiding sensor (OGS) is applied, that provides a high-precise information for *HST* body attitude control system (ACS) having four flywheels.

The *Herschel Space Observatory* has worked in the far infrared and submillimetre wavebands. This infrared space telescope with 3.5-m main mirror have completed research in March 2013, due to the limited capabilities of its cooling system. The *Planck Space Observatory* was designed with the directing tilled flat mirror with a light flow projective diameter of 1.5 m and is arranged on the survey platform. These observatories were placed in the 2nd Lagrange point of the Earth-Sun system.
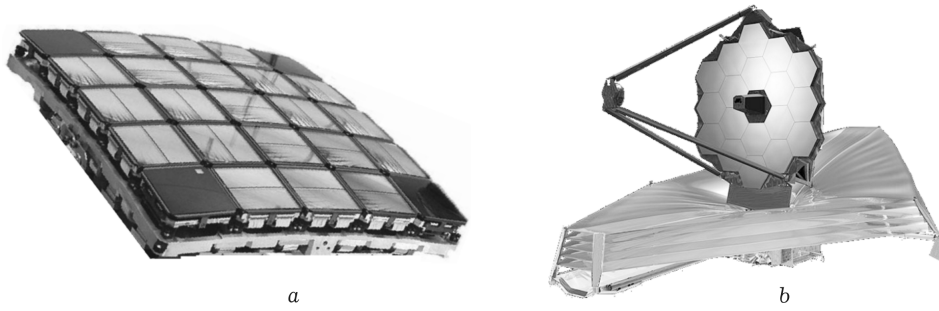
Figure 1.   The set of four OGSs at corners in the telescope focus surface (a) and the James Webb space telescope (b)

The *Kepler Space Observatory* was launched on a heliocentric orbit, its telescope has the 1.4-meter primary mirror. The focal surface of this telescope is made up of 42 CCDs at 2200×1024 pixels, Fig. 1a. The attitude stability is the primary factor for achieving the photometric precision. The requirement is to achieve a short-term accuracy of $3\sigma \approx 0.1$ arc sec relative to each of three axes over a time interval of up to 16 hours. To prevent the long-term drifts, four OGSs are mounted in the scientific focal surface at four corners, see Fig.1a.

The (*JWST*), Fig. 1b, was launched December 25, 2021. It is the space observatory optimized for observations in the infrared and is a scientific successor to the *HST*. The *JWST* primary mirror is the 6.5 meter diameter gold coated beryllium reflector with a collecting area of 25 m^2. Here, the OGS is applied to stabilize the telescope line-of-sight during scientific observations.

The OGS measurements are used to define the *JWST* body orientation and control the adjusting mirror – an image motion compensator (IMC). In the *JWST*, for the first time, the simultaneous operation of the ACS and the image motion stabilization system built into the telescope was implemented, when the required accuracy is obtained by the *nonius way*:

I cascade – angular stabilization of the *JWST* body;

II cascade – stabilization of an image *position* in the focal surface using angular movements of the IMC.

It should be noted here that the nonius method and embedded system for an image *position* stabilization in a space astronomical telescope were invented almost 50 years ago in the USSR [Dul'kin and Somov, 1975].

In this paper we consider an Earth-surveying satellite equipped with a telescope [Somov et al., 1999; Somov et al., 2022] and CCD matrices of the optoelectronic converters (OECs) into its focal surface. These matrices work in mode of the time delay and integration (TDI) when an observing given the Earth surface parts by a set of routes for their scanning [Somov et al., 2021].

The ACS of a maneuvering observation satellite has unique requirements for accuracy when a *scanning optoelectronic observing*.

The paper objectives are to develop algorithms for discrete filtering, offset guiding and analysis of the image motion *velocity* (IMV) as well as methods for verification of the embedded IMV stabilization system.

3   Mathematical Modeling of Physical Hysteresis

Fundamentally two types of the hysteresis relations are singled out in physical mediums: with index of a *limiting static loop* in negative direction (type $\mathcal{A}$, clockwise, Fig. 2a) and with index of this loop in positive direction (type $\mathcal{B}$, counter-clockwise, Fig. 2b).
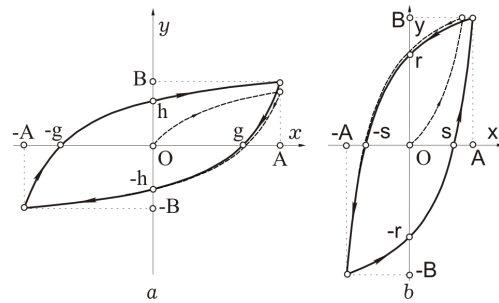

Figure 2.   Two types of hysteresis in physical mediums

It is important to distinguish a physical meaning of the arguments x and y for multi-valued hysteresis function $y = F_h(q_f, x)$ with a set q_f of both parameters and initial conditions. For example, *flexible-plastic* micro-deformations [Palmov, 1976] in an *internal* friction theory under notation $x = \varepsilon$ (mechanical deformation) and $y = \sigma$ (mechanical strength) are represented by the type $\mathcal{A}$ hysteresis relation. Note that in the theory of *external* friction theory the flexible-plastic micro-deformations have also such type hysteresis relation, if a variable x is a small line or angular displacement, and a variable y is respectively a friction force or torque, as in famous *Dahl*-type solid friction model [Dahl, 1976].

Ferro-magnetic hysteresis is presented by a $\mathcal{B}$-type multifunction (see Fig. 2b), if in the capacity of a forcing variable there is assumed $x = H$ (magnetic field strength) and as an output variable – a function $y = B$ (magnetic displacement).

The *dielectric* hysteresis also has the same type if a forcing function there is assumed a variable $x = E$ (electric field strength), and a output – a function $y = P$ (polarization of the piezoelectric material).

The $\mathcal{A}$-type hysteresis relation $y = F_h(\cdot, x)$, Fig. 2a, is transformed in a function $y = \Phi_h(q_\phi, x)$ of $\mathcal{B}$-type, Fig. 2b by the "mirror reflection" respect to an ordinate with a next rotation of obtained image on the angle $-\pi/2$ clockwise and renaming the coordinate axes as $x = y$ and
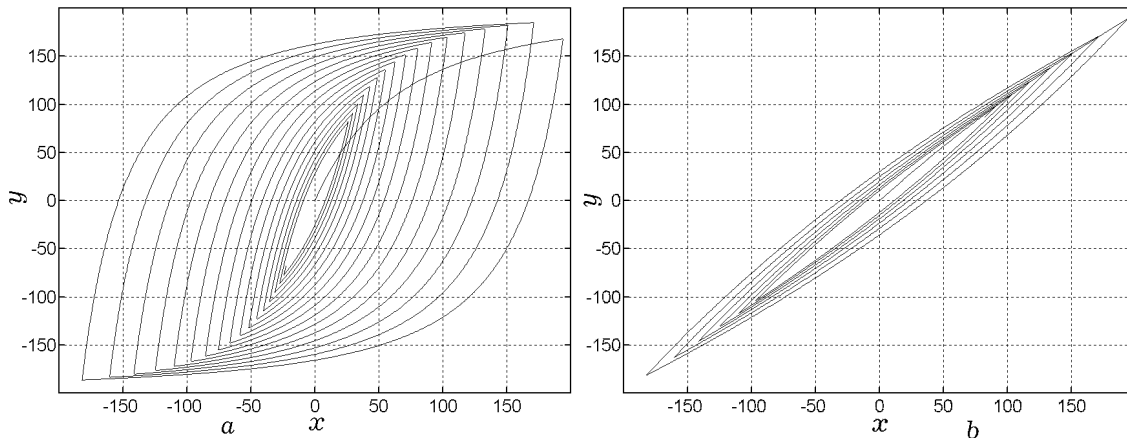
Figure 3.   The hysteresis function $y = F_h(\cdot, x)$ when $x(t) = A \exp(-\xi \omega\, t) \sin(\omega\, t)$, $A = 200$, $\xi = 0.2$, $\omega = 10$ 1/s: (a) $a_h = 200$, $k = 0.75\,10^{-3}, p = 0.1, \tilde{p} = 10^{-3}$;   (b) $a_h = 2000, k = 0.15\,10^{-6}, p = 2, \tilde{p} = 2.5\,10^{-3}$.

$y = x$. Moreover, for *limiting hysteresis loop* the coordinates of characteristic points (see Fig. 2) are transformed in such obvious way: $\mathsf{B} = \mathsf{A}; \mathsf{A} = \mathsf{B}$ and $\mathsf{r} = \mathsf{g}; \mathsf{s} = \mathsf{h}$. This method is well known, often is used in the *internal friction theory* [Kochneva, 1979]). It permits to study of only one type of hysteresis relation, in the capacity of which later on there is assumed the type $\mathcal{A}$, see Fig. 2a.
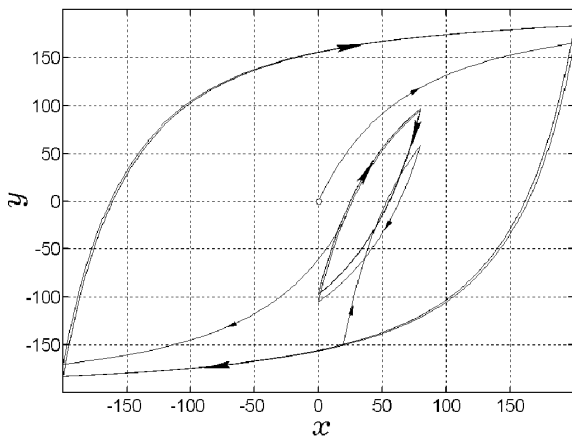

Figure 4.   Results of a hysteresis model testing

Assume that $x(t)$ is a real continuous and piecewise-differetiated function for $t \in \mathrm{T}_{t_0} \equiv [t_0, +\infty)$ and let there be values $\check{x}_\nu = x(t_\nu)$ of the function in the time moments t_ν, $\nu \in \mathbb{N}_0 \equiv [0, 1, 2, \cdots)$, when *last* changing *sign* of speed $x(t)$, namely $\dot{x}(t)$, was happened, e.g. $\check{x}_\nu \equiv x(t_\nu)|t_\nu : \mathrm{sign}\,\dot{x}(t_\nu + 0) \neq \mathrm{sign}\,\dot{x}(t_\nu - 0)$.

A *local function* $\tilde{x}_\nu(t)$ on each *local* time semi-interval $\mathrm{T}_\nu \equiv [t_\nu, t_{\nu+1})$ is introduced as

$$\tilde{x}_\nu(t) = x(t) - \check{x}_\nu \; \forall t \in \mathrm{T}_\nu,$$

and the *nonlinear functionally-parametrized* coefficient

$$k_\nu \equiv k_\nu(x(t)) \equiv k_\nu(k, p, \tilde{p}, \tilde{x}_\nu)$$

of the *hysteresis function shape* is defined in the form

$$k_\nu(x(t)) = k(1 - (1 - p)\exp(-\tilde{p}|\tilde{x}_\nu|)), \; t \in \mathrm{T}_\nu,$$

where $k, p, \tilde{p}$ are the constant positive parameters. For initial condition $x_0 \equiv x(t_0)$ the *normed* hysteresis func-

tion $r(t) = \mathrm{Hst}(\cdot, x(t))$ with restriction on its mo-dule by a constant parameter $\alpha_h > 0$, namely

$$r(t) \;=\; \mathrm{Hst}(a_h, \alpha_h, k_\nu(x(t)), r_o, x(t))$$

with condition $r(t_0) \equiv r_o = \mathrm{Hst}(a_h, \alpha_h, k_\nu(x_0), r_o, x_0)$, is defined as a *right-sided* solution of the equations

$$\mathrm{D}^+ r = \begin{cases} k_\nu\,|r - a_h \mathrm{sign}\,\dot{x}(t)|^{\alpha_h}\,\dot{x}(t) & |r| < a_h; \\ 0 & |r| \geq a_h; \\ r(t_0 + 0) = r_o, \end{cases} \quad (1)$$

where D^+ is symbol of a *right derivative* with respect to a time [Somov, 2000]. In relation (1) differential equation has a *discontinuous* right side and *ambiquitely* depends on input function $x(t)$ and its speed $\dot{x}(t)$ depends on all own *pre-history*, which is expressed by functional $k_\nu(x)$. Finally, at initial condition $y_o \equiv y_0 = y(t_0)$ for $x = x_0$ the hysteresis function $y(t)$ is defined as

$$y(t) \equiv m\,\mathrm{Hst}(a_h, \alpha_h, k_\nu, r_o, x(t))$$

with $r_o \equiv y_o/m$ and a constant scale coefficient $m > 0$.

In developed model (1) a parameter $\tilde{p}$ determines on the whole a degree of convergence for a trajectory $y(t) = F_h(\cdot, x(t))$ in the plane xOy on symmetric limiting static loop under a harmonic forcing function $x(t) = A \sin \omega t$ with fixed values A, ω and initial condition $y_o = y_0$ when $|y_o|/m < a_h$, see also Fig. 3. For this model all standard requirements are realized, including the famous requirements on a model *vibro-correctness* [Krasnosel'skii and Pokrovskii, 1989] as well as on a *frequency independence* [Sorokin, 1960] and a fine return on a main symmetric limiting hysteresis loop after a short-term passage on a displaced local hysteresis loop [Palmov, 1976; Kochneva, 1979]. Last property is verified by Fig. 4 for the hysteresis model (1) with parameters $m = 1$, $\alpha_h = 1.5$, $a_h = 200$, $k = 5.125\,10^{-4}$, $p = 2$, $\tilde{p} = 0.75\,10^{-3}$ when the forcing function $x(t)$ has the following form

$$x(t) = \begin{cases} A \sin \omega_1 t & (0 \leq t < \tau_1)\&(\tau_2 \leq t \leq \tau_3); \\ B(1 + \sin \omega_2 t) & \tau_1 \leq t < \tau_2, \end{cases}$$

$A = 200$; $B = 40$; $\omega_1 = 1$; $\omega_2 = 5$; $\tau_3 = 40$;
$\tau_1 \equiv 5\pi - \tau^*$; $\tau_2 = 7\pi - \tau^*$; $\tau^* \approx 0.03415\pi$.
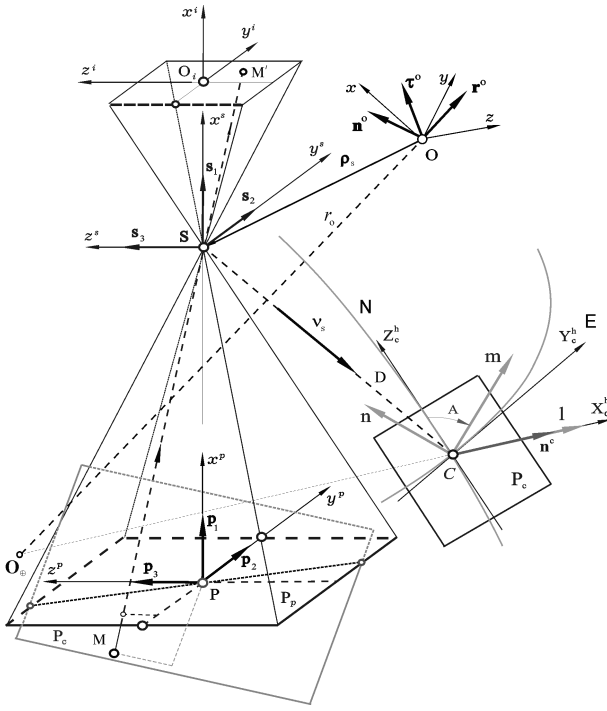
Figure 5.   The reference frames for a space optoelectronic surveying

4   The IMV Stabilization System

We use the following bases and reference frames:
- inertial reference frame (IRF) $\mathbf{I}_{\oplus}$ ($O_{\oplus}X^I_e Y^I_e Z^I_e$);
- geodesic Greenwich reference frame $\mathbf{E}_e$ rotated in the IRF by angular velocity vector $\boldsymbol{\omega}_{\oplus} \equiv \boldsymbol{\omega}_e$;
- geodesic horizon reference frame $\mathbf{E}^h_e$: axis $C\,X^h_e$ is the local vertical, axes $C\,Y^h_c$ and $C\,Z^h_c$ lie in the local horizon plane and directed to local East (E) and local North (N), respectively, Fig. 5;
- body reference frame (BRF) $\mathbf{B}$ ($Oxyz$) with the origin in the spacecraft mass center O;
- orbital reference frame (ORF) $\mathbf{O}$ ($Ox^o y^o z^o$): axis Oy^o lies in the orbit radius and axis Oz^o points in negative direction of the orbit normal, see Fig. 5;
- main sensor reference frame (SRF) $\boldsymbol{\mathcal{S}}$ (S $x^s y^s z^s$) with origin in point S – the center of optical projection, Fig. 5;
- an image field reference frame $\boldsymbol{\mathcal{F}}$ ($O_i x^i y^i z^i$) with origin in center O_i of telescope focal plane $y^i O_i z^i$, Fig. 5;
- visual reference frame $\mathbf{V}$ ($O_v x^v y^v z^v$) with the origin in center O_v of main OEC linear array.

The BRF orientation in the IRF is defined by quaternion $\boldsymbol{\Lambda} = (\lambda_0, \boldsymbol{\lambda})$, $\boldsymbol{\lambda} = \{\lambda_1, \lambda_2, \lambda_3\}$, and with respect to the ORF – by column $\boldsymbol{\phi} = \{\phi_i\}$ ($i = 1, 2, 3 \equiv 1 \div 3$) of Euler-Krylov angles ϕ_1 (roll), ϕ_2 (yaw) and ϕ_3 (pith).

We use also a vector of modified Rodrigues parameters (MRP) $\boldsymbol{\sigma} = \mathbf{e}\tan(\Phi/4)$ with Euler unit vector $\mathbf{e}$ and angle Φ of own rotation. The quaternion $\boldsymbol{\Lambda}$ and the vector MRP $\boldsymbol{\sigma}$ are uniquely related by explicit relations.

Let vectors $\boldsymbol{\omega} = \{\omega_i\}$, $\mathbf{r} = \{r_i\}$ and $\mathbf{v} = \{v_i\}$ are the body angular velocity, position and progressive velocity. Assume that $\boldsymbol{\Lambda}^p(t)$ and $\boldsymbol{\omega}^p(t)$ present the spacecraft body programmed motion. The error quaternion is $\mathbf{E} = (e_0, \mathbf{e})$

$= \tilde{\boldsymbol{\Lambda}}^p(t) \circ \boldsymbol{\Lambda}$ with vector $\mathbf{e} = \{e_i\}$, the attitude error matrix is $\mathbf{C}^e = \mathbf{I}_3 - 2[\mathbf{e}\times]\mathbf{Q}^t_e$ with $\mathbf{Q}_e = \mathbf{I}_3 e_0 + [\mathbf{e}\times]$ and the attitude error vector is $\delta\boldsymbol{\phi} = \{\delta\phi_i\} \equiv \{2e_0 e_i\}$. The angular velocity error vector is $\delta\boldsymbol{\omega} = \boldsymbol{\omega} - \mathbf{C}^e\boldsymbol{\omega}^p(t)$. Here and further symbols $\circ$, $\tilde{}$ for quaternions, $\langle\cdot,\cdot\rangle$, $\times$, $\{\cdot\} \equiv \mathrm{col}(\cdot)$, $[\cdot] \equiv \mathrm{line}(\cdot)$ for vectors and $[\cdot\times]$, $(\cdot)^t$, $\lceil\cdot\rfloor \equiv \mathrm{diag}(\cdot)$ for matrices are conventional notations.

Resolution of a space Earth-surveying telescope depends to a big extent on a remote sensing spacecraft spatial angular motion along the survey route. To obtain a high quality image it is reasonable to calculate the image longitudinal velocity (ILV) V^i_y in a telescope focal plane. It is also necessary that for an image cross velocity (ICV) V^i_z the condition $|V^i_z| \leq V^i_d$ was fulfilled with a constant value V^i_d. We assume that in the SRF vector columns $\boldsymbol{\omega}^s_e$ and $\mathbf{v}^s_e$ present angular and forward velocity of a satellite with respect to the GRF, matrix $\tilde{\mathbf{C}} = \| \tilde{c}_{ij} \|$ defines the SRF orientation also with respect to the GRF, and scalar function $D(t)$ presents the oblique range of observation.

For any point at the telescope focal plane the longitudinal $\tilde{V}^i_y(\tilde{y}^i, \tilde{z}^i)$ and cross $\tilde{V}^i_z(\tilde{y}^i, \tilde{z}^i)$ components of normed IMV vector $\tilde{\mathbf{V}}^i = \{\tilde{V}^i_y, \tilde{V}^i_z\}$ are calculated by the following relation

$$\begin{bmatrix} \tilde{V}^i_y \\ \tilde{V}^i_z \end{bmatrix} = \begin{bmatrix} \tilde{y}^i & 1 & 0 \\ \tilde{z}^i & 0 & 1 \end{bmatrix} \begin{bmatrix} q^i \tilde{v}^s_{e1} - \tilde{y}^i \omega^s_{e3} + \tilde{z}^i \omega^s_{e2} \\ q^i \tilde{v}^s_{e2} - \omega^s_{e3} - \tilde{z}^i \omega^s_{e1} \\ q^i \tilde{v}^s_{e3} + \omega^s_{e2} + \tilde{y}^i \omega^s_{e1} \end{bmatrix}. \quad (2)$$

Here $\tilde{y}^i = y^i / f_e$ and $\tilde{z}^i = z^i / f_e$ are normed focal coordinates of indicated point where f_e is the telescope equivalent focal distance, function $q^i = 1 - (\tilde{c}_{21}\tilde{y}^i + \tilde{c}_{31}\tilde{z}^i)/\tilde{c}_{11}$ and components $\tilde{v}^s_{ei}(t)$ of normed forward velocity vector $\tilde{\mathbf{v}}^s_e(t) = \{v^s_{ei}(t), i = 1 \div 3\}$ are computed by relation $\tilde{v}^s_{ei}(t) = v^s_{ei}(t)/D(t)$.

The vector relation (2) is applied for an analytical synthesis of the guidance basic laws of the Earth surveying satellites when tracked observation.
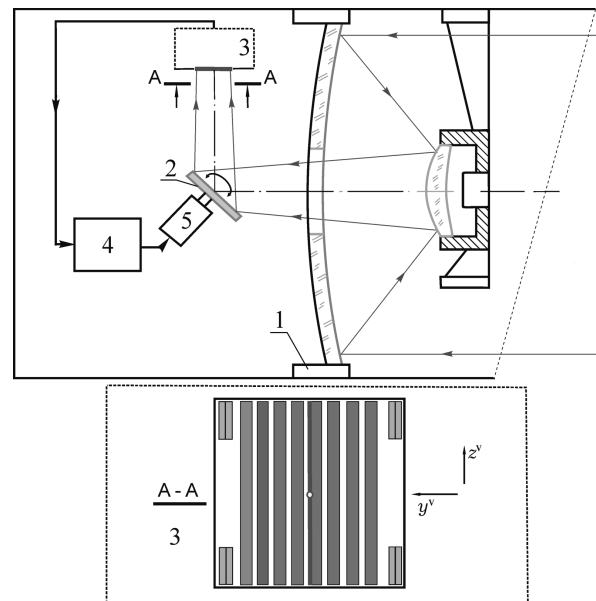

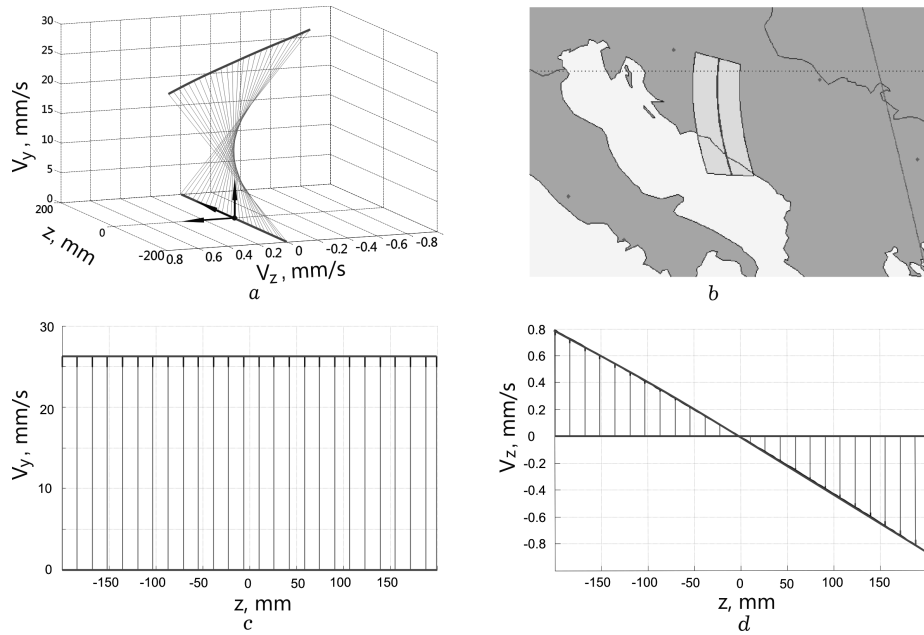Figure 6.   Scheme of a system for the IMV stabilization

Figure 7.   Distribution of the ILV and ICV along the main central line in a focal plane when a guidance law with the ILV alignment:
the spatial picture (*a*),   representation of the survey route on a map (*b*),   the ILV distribution (*c*) and the ICV distribution (*d*)

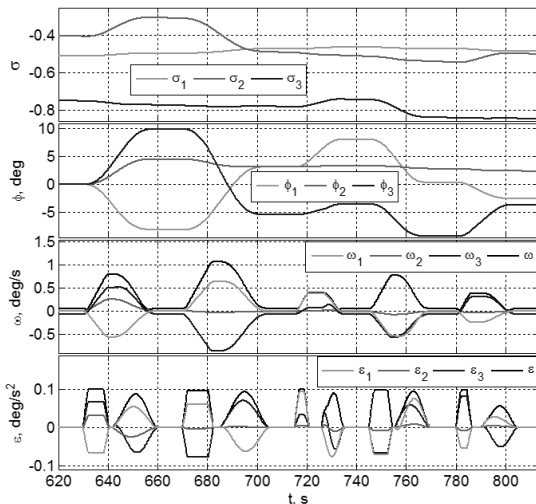Figure 8.   The space Earth-observing routes on a map

Figure 9.   The guidance law when a scanning Earth-survey

Principal idea of embedded system for the IMV stabilization on the OECs set is presented in Fig. 6. Here in objective (1) on Ritchey-Chretien scheme we have IMC (2) in the form of a plane diagonal moving mirror; the fine OGS (3) by an image motion *velocity* in center of the telescope focal plane (marked by red) – the sensor is implemented by digital processing signals of four etalon OECs with TDI (marked by blue) and fixed in four corners of the OEC structure in the telescope focal surface; converter (4) of digital control signals of the piezo drive (5) for small angular displacements of the IMC (2).

When scanning observation of the Earth surface, it is necessary to provide a given movement velocity of optical images strictly along the OEC columns for the accumulation of moving electronic images. Here, a strict synchronization in the movements of optical and electronic images is required both in the longitudinal and transverse directions for given points in the OESs of CCD matrices. Moreover, the output signals are formed in a "sliding window" with K rows of the current accumulated electronic image along the corresponding columns.

The main angular motion of the telescope body is given by the guidance law formed in a spacecraft ACS. The physical distribution of the IMV vector components $\mathbf{V}^i = \{V_y^i, V_s^i\}$ along the main central line in the telescope focal plane is represented in Fig. 7 when the best guidance law with the ILV alignment is applied.

Assume that an Earth-observing satellite is moving on sun-synchronous orbit with altitude 720 km and it fulfills the task for the scanning optoelectronic observations of Benevento, Rome, Florence, Padua and Munich with duration of 10 s each route, see Fig. 8. Synthesised guidance law is presented in Fig. 9, where components of
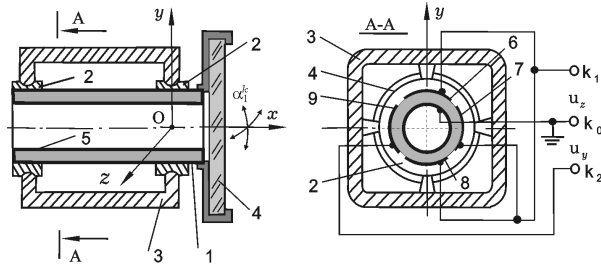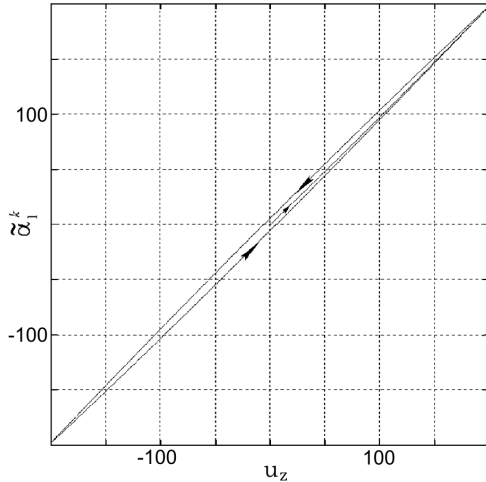
Figure 10.   Scheme of the IMC piezoceramic drive

Figure 11.   The piezo drive normed hysteresis in the working mode

vectors $\boldsymbol{\sigma}(t)$, $\boldsymbol{\phi}(t)$, $\boldsymbol{\omega}(t)$ and $\boldsymbol{\varepsilon}(t)$ are marked by blue on roll, green on yaw and red on pitch, and modules of vectors $\boldsymbol{\omega}(t)$ and $\boldsymbol{\varepsilon}(t)$ are marked by black.

Scheme of developed piezoceramic drive is presented in Fig. 10. The piezo drive has a tubular design [Somov, 1974] with the possibility of bending in two orthogonal planes of the piezoceramic element (PCE) (1). The PCE is freely attached to the case (3) on the borders of two orthogonal planes by spacers (2). The IMC (4) is rigidly connected to the end of the PCE (1) such that its reflecting plane is orthogonal to the PCE axis.

The PCE has five electrodes: the general electrode (5) at its internal surface and 4 external electrodes (6) – (9) ordered along the PCE in such a way that the symmetry planes of the opposite electrodes are mutually orthogonal. The PCE longitudinal parts have contrary directions of the radial polarization under opposite electrodes.

When the control voltage is applied to the points $k_1 \& k_0$ (or the points $k_2 \& k_0$), then due to a reverse transverse piezo-effect, the PCE parts under electrodes 6&8 (or respectively under electrodes 7&9 are deformed in the contrary directions and, therefore, the PCE bends are happened at the relevant planes. So, the tubular piezoceramic element in Fig. 10 is equivalent to the controlled 2-DOF Hooke hinge [Somov, 1974].

For piezoceramic materials their hysteresis not exceeds 5% for electric field strength $|E^e| \le E^{em} = 2$ kV/cm.

At angular deviation α_1^k of IMC 4 in Fig. 10 the PCE *linear normed* static characteristic is appeared as $\tilde{\alpha}_1^k \equiv$

$\alpha_1^k / k_u^\alpha = u_z$, where $k_u^\alpha \equiv -(d_{31} l_p)/(2\sqrt{2} h_p \, r_p \, \lambda_t^p) > 0$, l_p, r_p and $h_p \ll r_p$ are the PCE's length, mean radius and a wall thickness at standard notation of the piezoceramic's parameters $d_{31} < 0$, $k_{31}^2 = d_{31}^2/(S_{11}^E \varepsilon_{33}^\sigma) < 1$ when the standard number λ_t^p is computed by relation

$$\lambda_t^p = (1 - 2\sqrt{2}\, k_{31}^2/(3\pi) + (h_p/r_p)^2 \,/12)/(1 - k_{31}^2) > 1.$$

For PCE wall thickness $h_p = 1$ mm, maximum voltage $u_z^m = 200$ V matches to electric field strength 2kV/cm, so the piezodrive's hysteresis not exceeds 3%, see Fig. 11.

The condition $mkpa_h^\alpha = 1$ is needed to take into account for *hysteresis* parameters m, a_h, α, k and p. For notation $E_q^p = (\pi/2)^4 E_e^p/4$, $E_e^p \equiv (S_{11}^E \lambda_t^p)^{-1}$ and $I_p \equiv \pi r_p^3 h_p$, in terms of *bending torques* the PCE's *static* $\mathcal{A}$-type hysteresis characteristic is presented in the form

$$(3E_q^p \, I_p/l_p) \, k_u^\alpha \, y(t) = k_z^k \, u_z(t); \quad y(t) = m \, r(t); \\ r(t) = \mathrm{Hst}(a_h, \alpha, k_\nu(x(t)), r_o, x(t)) \tag{3}$$

with $x(t) = \tilde{\alpha}_1^k$; $k_z^k = -3d_{31}(\pi/2)^5 (r_p/\lambda_t^p)^2/(4\sqrt{2} S_{11}^E)$, initial value $r_o = r(t_0) \equiv y_o/m = u_z(t_0)/m$ and mandatory concordance of initial conditions

$$r_o = \mathrm{Hst}(a_h, \alpha, k_\nu(x_0), r_o, x_0).$$

If $w_y(t, x)$ is a transverse displacement any point at the PCE's axis, then $\alpha_1^k(t) = \partial w_y(t, l_p)/\partial x$ and a curvature $\kappa_z(E_z(t), x) = \partial^2 w_y(t, x)/\partial x^2$ of the PCE's bending in *linear* theory is appeared as follows

$$\kappa_z(E_z^e(t), x) = -(d_{31}/(\sqrt{2}\, r_p \lambda_t^p)) \, E_z^e(t),$$

where $E_z^e(t) = u_z(t)/h_p$. For own PCE mass m_p and parameter $m_p^l \equiv m_p/l_p$, the well-known *wave equation*

$$m_p^l[\partial^2 \, w_y(t, x)/\partial t^2] + I_p E_e^p \, [\partial^4 \, w_y(t, x)/\partial x^4] = 0$$

has analytic solution via the normed Krylov functions.

By *first* partial frequency $\Omega_1^p = (\pi/l_p)^2 (I_p E_e^p/m_p^l)^{1/2}$ of own *bending* oscillations, the PCE has equivalent mass $m_e^p = (l_p/h_1^k)^2 m_p/32$, where h_1^k is a distance between the IMC mass center and point O, see Fig. 10. At own the IMC's mass m_1^k and moment of inertia J_1^k, the "IMC+PCE"-cluster has equivalent general mass $\mu_1^k \equiv J_1^k + (m_1^k + m_e^p)(h_1^k)^2$ in point O. A simplest *linear* piezo drive's dynamical model has the form

$$\mathrm{M}_1^{kr} + \mu_1^k(\ddot{\alpha}_1^k + \nu_1^k \Omega_1^k \dot{\alpha}_1^k + (\Omega_1^k)^2 \alpha_1^k) = k_z^k \, u_z(t), \tag{4}$$

where $\mathrm{M}_1^{kr}(t)$ is an inertia torque because of spacecraft attitude motion and $\nu_1^k = 2\xi_1^k$ with standard damping factor ξ_1^k. Taking into account relations (3) and (4), at condition $\mathrm{M}_1^{kr} = 0$ the piezo drive's *nonlinear hysteresis* model is appeared as follows

$$\mu_1^k[\ddot{\alpha}_1^k + \nu_1^k \Omega_1^k \dot{\alpha}_1^k + k_u^\alpha(\Omega_1^k)^2 y(t)] = k_z^k \, u_z(t); \\ y(t) = mr(t); \quad r(t) = \mathrm{Hst}(\cdot, x(t)); \quad x(t) = \alpha_1^k/k_u^\alpha \tag{5}$$

with concordance of initial conditions.

Both static and dynamic studies on identification of the piezoceramic drive hysteresis and damping parameters were carried out by careful research of nonlinear model (5) taking into account *experimental* data obtained in the
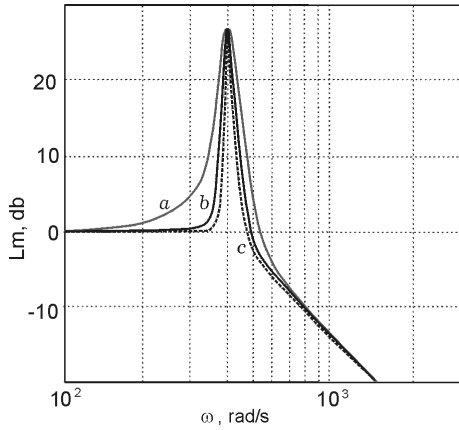
Figure 12. The piezo drive amplitude-frequency characteristics

late 1970s. Results of dynamic properties comparison at input command amplitude $u_z^m = 200$ V are presented in Fig. 12: (*a*) for model 4) with $\nu_1^k = 0.06$, (*b*) for model (5) with $\nu_1^k = 1.73\,10^{-3}$ and (*c*) with average experimental data. Here, the values of coefficient ν_1^k and parameters of the piezo drive hysteresis were chosen from the condition of matching the maximum value of the amplitude-frequency characteristics for all three models, see Fig. 12. When the embedded system works, precise stabilization is fulfilled for the longitudinal and cross IMVs with compensation of a frequency non-stability at replacing the electronic charges along columns of the information OECs marked by grey color in Fig. 6.

5 The Discrete Filtering and Offset Guiding

Four etalon matrices located in the telescope focal surface have two shifted OES lines, see Fig. 6. That makes it possible to determine the set of the IMV vector values in the etalon matrices and using the least squares method to calculate values $\tilde{\mathbf{V}}_p^i = \{\tilde{V}_{yp}^i, \tilde{V}_{zp}^i\}$ for four points $(\tilde{y}_p^i, \tilde{z}_p^i)$, $p = 1 \div 4$ – for the centers of four etalon matrices. Relation (2) is presented in the form

$$\{\tilde{V}_y^i, \tilde{V}_z^i\} = \tilde{\mathbf{Q}}^i(\tilde{y}^i, \tilde{z}^i) + \mathbf{P}^i(\tilde{y}^i, \tilde{z}^i)\{\boldsymbol{\omega}_{\mathrm{e}i}^s\},$$

$$\tilde{\mathbf{Q}}^i(\tilde{y}^i, \tilde{z}^i) = q^i\{\tilde{v}_{\mathrm{e}1}^s\tilde{y}^i + \tilde{v}_{\mathrm{e}2}^s, \ \tilde{v}_{\mathrm{e}1}^s\tilde{z}^i + \tilde{v}_{\mathrm{e}3}^s\};$$

$$\mathbf{P}^i(\tilde{y}^i, \tilde{z}^i) = \begin{bmatrix} -\tilde{z}^i & \tilde{y}^i\tilde{z}^i & -(1 + (\tilde{y}^i)^2) \\ \tilde{y}^i & 1 + (\tilde{z}^i)^2 & -\tilde{y}^i\tilde{z}^i \end{bmatrix}.$$

For center $(\tilde{y}_p^i, \tilde{z}_p^i)$ each etalon OEC matrix we have obtained the relation $\mathbf{Q}_p^i = \mathbf{P}_p^i\boldsymbol{\omega}_{\mathrm{e}}^{sp}$, where $\boldsymbol{\omega}_{\mathrm{e}}^{sp} = \{\omega_{\mathrm{e}i}^{sp}\}$, $\mathbf{Q}_p^i = \tilde{\mathbf{V}}_p^i - \tilde{\mathbf{Q}}^i(\tilde{y}_p^i, \tilde{z}_p^i)$ and $\mathbf{P}_p^i = \mathbf{P}^i(\tilde{y}_p^i, \tilde{z}_p^i)$.

On the whole for the centers of all four etalon OEC matrices we have common relation $\mathbf{Q}_\Sigma^i = \mathbf{P}_\Sigma^i\boldsymbol{\omega}_{\mathrm{e}}^{sp}$, where column $\mathbf{Q}_\Sigma^i = \{\mathbf{Q}_p^i\}$ and matrix $\mathbf{P}_\Sigma^i = \{\mathbf{P}_p^i\}$.

We have computed estimation $\hat{\boldsymbol{\omega}}_{\mathrm{e}}^s = (\mathbf{P}_\Sigma^i)^{\#}\mathbf{Q}_\Sigma^i$ of angular velocity vector by the least-squares method on the space pictures of terrestrial targets with pseudo-inverted matrix $(\mathbf{P}_\Sigma^i)^{\#}$. Next, the vector evaluation $\hat{\boldsymbol{\omega}}_{\mathrm{e}}^s$ is applied for a computing in real time the normed IMV vector $\tilde{\mathbf{V}}_m^i = \{\tilde{v}_{\mathrm{e}2}^s - \hat{\omega}_{\mathrm{e}3}^s, \tilde{v}_{\mathrm{e}3}^s + \hat{\omega}_{\mathrm{e}2}^s\}$ in center O_i of the telescope focal plane by analysis of the picture flow with

terrestrial targets. Center of the information OEC matrices corresponds to point O_{v}, see red line and its center in Fig. 6. As a result, we have obtained vector $\tilde{\mathbf{V}}_m^i$ of *measured* IMV in center of the telescope focal plane during spacecraft orbital flight.

In described procedure the disparity analysis is fulfilled for pictures of arbitrary terrestrial targets. The pictures are obtained at two next successive OEC lines in the etalon matrices. The procedure has large computational complexity, therefore here it is rationally to carry out the parallel calculations using an individual microprocessor for each of the four OEC etalon matrices that together make up the fine offset guiding sensor with respect to the image motion velocity vector.
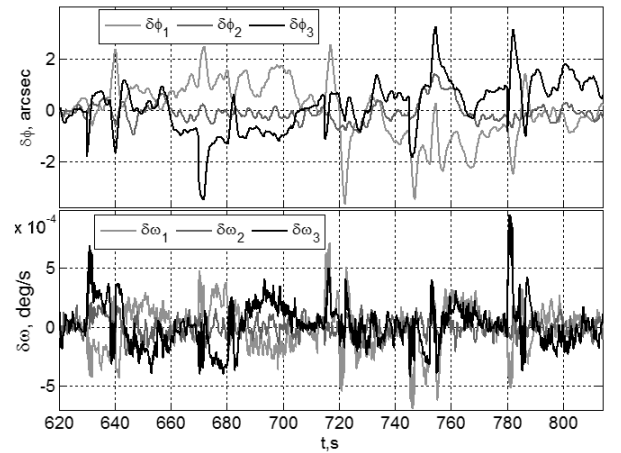

Figure 13. The spacecraft attitude and angular velocity errors

6 Simulation of the IMV Stabilization System

When observing parts of the Earth in Fig. 8, the SC guidance law in Fig. 9 has five scanning routes, namely Benevento, $\forall t \in [660, 670)$ s; Rome, $\forall t \in [705, 715)$ s; Florence, $\forall t \in [735, 745)$ s; Padua, $\forall t \in [770, 780)$ s and Munich, $\forall t \in [805, 815)$ s with four rotational maneuvers in between. The SC attitude and angular velocity errors during while scanning observations are represented in Fig. 13.

Let be given vector $\tilde{\mathbf{V}}_*^i = \{\tilde{V}_{y*}^i, \tilde{V}_{z*}^i\} \equiv \{\tilde{V}_{y*}^i, 0\}$ of required normed IMV in center of the telescope focal plane, and vector $\tilde{\mathbf{V}}^i = \{\tilde{V}_y^i, \tilde{V}_z^i\}$ presents the real IMV in the same point. For the IMC *fixed* nominal angular position the error vector $\Delta\tilde{\mathbf{V}}^i$ of the normed IMV in center O_{v} of the OEC information matrices (see red line in Fig. 6) is computed by relation $\Delta\tilde{\mathbf{V}}^i \equiv \{\Delta\tilde{V}_y^i, \Delta\tilde{V}_z^i\} = \tilde{\mathbf{V}}_a^i - \tilde{\mathbf{V}}_*^i$, where $\tilde{\mathbf{V}}_a^i \equiv \{\tilde{V}_{ya}^i, \tilde{V}_{za}^i\}$ is the normed IMV vector in the same center due to the telescope body *attitude* control during the scanning Earth observation.

If the IMC angular position *changes* relative the telescope body by its piezoceramic drive, then vector of the IMV stabilization error $\delta\Delta\tilde{\mathbf{V}}^i = \{\delta\Delta\tilde{V}_y^i, \delta\tilde{V}_z^i\}$ is forming taking into account both the IMC movements and coefficients of optical reduction. Moreover, the OGS algorithms and computed normed IMV vectors $\Delta\tilde{\mathbf{V}}^i, \tilde{\mathbf{V}}_m^i$
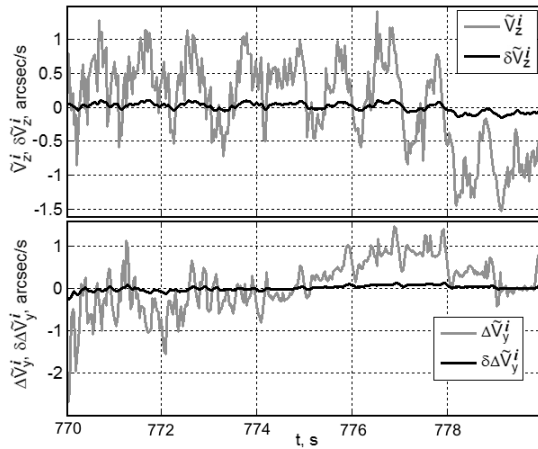
Figure 14.   Errors when the IMV stabilization system operation

allow to compute the IMV error vector $\delta\Delta\tilde{\mathbf{V}}^i$ taking into account the IMV stabilization system's operation. The embedded system is closed – the IMV error vector $\delta\Delta\tilde{\mathbf{V}}^i$ is an input signal for piezoceramic drive and variation of the IMC position results in elimination of indicated error simultaneously in both the OGS based on digital processing signals from four OEC etalon matrices and the OEC information matrices. When the IMV stabilization system works, recurrent filtering of the normalized error vector $\delta\Delta\tilde{\mathbf{V}}^i$ is applied with frequency 32 Hz as well as astatic digital control law for the IMC piezo drive with frequency 16 Hz. This control law was synthesized taking into account a time delay [Somov, 2001], it has bandwidth 5.7 Hz. In Figure 14 we present errors on components of normed IMV vector without switch in (blue) and at operation (red) of the embedded system.

7 Terrestrial and In-flight Verification

Terrestrial verification of the embedded system is carried out by original scheme: the telescope body is fixed in a table, its optical axis is directed to large-scale full-HD monitor with the *moving* images of terrestrial targets. These images are generated by a computer simulation of the spacecraft spatial motion. In-flight verification is carried out during a time period of the spacecraft tests on terrestrial polygons, details see in [Somov et al., 2022].

8 Conclusions

A universal approach to modeling hysteresis in physical media based on multi-valued differential equations with a discontinuous right-hand side was presented. The main engineering relationships for calculating the parameters of a piezoceramic drive are given, taking into account its physical hysteresis. Basic algorithms for the offset guiding and signal processing were developed, nonlinear studies of the embedded system were carried out and the results of its effectiveness for accurate stabilization of the image motion velocity are presented.

Acknowledgements

References

Dahl, P. (1976). Solid friction damping of mechanical vibrations. *AAAI Journal*, **14** (12), pp. 1675–1682.

Derler, P., Lee, E., and et al. (2012). Modeling cyber–physical systems. *Proc. IEEE*, **100** (1), pp. 13–28.

Dragan, D. (2006). Hysteresis in piezoelectric and ferroelectric materials. In *The Science of Hysteresis*, vol. 1, chapter 4, pp. 337–465. Elsevier, Amsterdam.

Dul'kin, L. and Somov, Y. (1975). *The astronomical telescope with the precision image position stabilization. The USSR Patent* 558595. In Russian.

Kochneva, L. (1979). *Internal Friction in Solid Bodies at Oscillations*. Nauka, Moscow. In Russian.

Krasnosel'skii, M. and Pokrovskii, A. (1989). *Systems with Hysteresis*. Springer-Verlag, Berlin - Heidelberg.

Palmov, V. (1976). *Oscillations of Flexible-plastic Bodies*. Nauka, Moscow. In Russian.

Panovko, Y. (1960). *Internal Friction at Oscillations of Flexible Systems*. Fizmatgiz, Moscow. In Russian.

Somov, Y. (1974). *The device for the ray deflection. The USSR Patent* 543301. In Russian.

Somov, Y. (2000). Model of physical hysteresis and control of an image motion oscillations at a large space telescope. In *Proc. 2nd Intern. Conf. on Control of Oscillations and Chaos*, vol. 1, St. Petersburg, pp. 70–75.

Somov, Y. (2001). Robust stabilization of flexible spacecraft under conditions of incomplete discrete measurements and control delay. *J. Comput. Syst. Sci. Int.*, **40** (2), pp. 287–307.

Somov, Y. (2004). Modeling physical hysteresis and control of a fine piezo drive. In *Proc. 1st IEEE/IUTAM Intern. Conf. on Physics and Control*, vol. 4, Saint Petersburg, pp. 1189–1194.

Somov, Y., Butyrin, S., Matrosov, V., and et al. (1999). Ultra-precision attitude control of a large low-orbital space telescope. *CEP*, **7** (7), pp. 1127–1142.

Somov, Y., Butyrin, S., and Somov, S. (2021). Dynamics of an autonomous spacecraft control system at initial transition to a tracking mode. *Cybern. Phys.*, **10** (3), pp. 185–190.

Somov, Y., Butyrin, S., Somov, S., and Somova, T. (2022). Nonius stabilization of an image motion velocity in the telescope of an Earth observing satellite. *Math. Eng. Sci. Aerosp.*, **13** (1), pp. 51–62.

Sorokin, E. (1960). *On Internal Friction Theory for Oscillations of Flexible Systems*. Gosstroyizdat, Moscow.

Visintin, A. (2006). Mathematical models of hysteresis. In *The Science of Hysteresis*, vol. 1, chapter 1, pp. 1–123. Elsevier/Academic Press, Amsterdam.

Visintin, A. (2014). Ten issues about hysteresis. *Acta Appl. Math.*, **132**, pp. 635–647.

Yu, Z., Wu, Y., Fang, Y., and Sun, H. (2020). Modeling and compensation of hysteresis in piezoelectric actuators. *Heliyon*, **6** (5), pp. 1e03999.

Zhang, G., Zhang, C., and Gu, J. (2012). A memory-based hysteresis model in piezoelectric actuators. *JCSE*, **2012** (498590), pp. 1–7.